Astronomy & Astrophysics

The distance and size of the red hypergiant NML Cygni from VLBA and VLA astrometry

B. Zhang[1,2], M. J. Reid[3], K. M. Menten[1], X. W. Zheng[4], and A. Brunthaler[1,5]

[1] Max-Plank-Institut für Radioastronomie, Auf dem Hügel 69, 53121 Bonn, Germany
   e-mail: bzhang@mpifr.de
[2] Shanghai Astronomical Observatory, Chinese Academy of Sciences, 80 Nandan Road, 200030 Shanghai, PR China
[3] Harvard-Smithsonian Center for Astrophysics, 60 Garden Street, Cambridge, MA 02138, USA
[4] Department of Astronomy, Nanjing University, 22 Hankou Road, 210093 Nanjing, PR China
[5] National Radio Astronomy Observatory, Socorro, NM 87801, USA

ABSTRACT

Context. The red hypergiant NML Cyg has been assumed to be at part of the Cyg OB2 association, although its distance has never been measured directly. A reliable distance is crucial to study the properties of this prominent star. For example, its luminosity, and hence its position on the H-R diagram, is critical information to determine its evolutionary status. In addition, a detection of the radio photosphere would be complementary to other methods of determining the stellar size.
Aims. We aim to understand the characteristics of NML Cyg with direct measurements of its absolute position, distance, kinematics, and size.
Methods. We observe circumstellar 22 GHz H_2O and 43 GHz SiO masers with the Very Long Baseline Array to determine the parallax and proper motion of NML Cyg. We observe continuum emission at 43 GHz from the radio photosphere of NML Cyg with the Very Large Array.
Results. We measure the annual parallax of NML Cyg to be 0.620 ± 0.047 mas, corresponding to a distance of $1.61^{+0.13}_{-0.11}$ kpc. The measured proper motion of NML Cyg is $\mu_x = -1.55 \pm 0.42$ mas yr^{-1} eastward and $\mu_y = -4.59 \pm 0.41$ mas yr^{-1} northward. Both the distance and proper motion are consistent with that of Cyg OB2, within their joint uncertainty, confirming their association. Taking into consideration molecular absorption signatures seen toward NML Cyg, we suggest that NML Cyg lies on the far side of the Cyg OB2 association. The stellar luminosity revised with our distance brings NML Cyg significantly below the empirical luminosity limit for a red supergiant. We partially resolve the radio photosphere of NML Cyg at 43 GHz and find its diameter is about 44 mas, suggesting an optical stellar diameter of 22 mas, if the size of radio photosphere is 2 times the optical photosphere. Based on the position of circumstellar SiO masers relative to the radio photosphere, we estimate the absolute position of NML Cyg at epoch 2008.868 to be $\alpha_{J2000} = 20^h46^m25\overset{s}{.}5382 \pm 0\overset{s}{.}0010$, $\delta_{J2000} = 40°06'59\overset{''}{.}379 \pm 0\overset{''}{.}015$. The peculiar motions of NML Cyg, the average of stars in Cyg OB2, and four other star-forming regions rules out that an expanding "Strömgren sphere" centered on Cyg OB2 is responsible for the kinematics of the Cygnus X region.

Key words. astrometry – masers – parallaxes – proper motions – stars: individual: NML Cyg – supergiants

1. Introduction

NML Cyg is one of the most massive and luminous red hypergiants. It is a semi-regular star with period ≈1000 days (Denisenkova et al. 1988; Monnier et al. 1997) and has been suggested to be associated with Cyg OB2, possibly the largest stellar association in the Galaxy (Habing et al. 1982; Morris & Jura 1983). Previous distance estimates for NML Cyg have been mainly based on the assumption that it is at the distance with Cyg OB2. Even so, the distance to Cyg OB2 is hard to determine accurately by photometry and spectroscopy, due to difficulty in calibrating spectral types and luminosities. Previous investigators have derived distance moduli of 10.8–11.6 (Johnson & Morgan 1954; Reddish et al. 1966; Walborn 1973; Abbott et al. 1981; Torres-Dodgen et al. 1991; Massey & Thompson 1991; Hanson 2003; Kharchenko et al. 2005), corresponding to distances of 1.45–2.10 kpc to Cyg OB2. These values are marginally different from 1.22 ± 0.3 kpc to NML Cyg determined by Danchi et al. (2001), based on the comparison of Doppler velocities and proper motions of two discrete dust shells around NML Cyg measured with interferometry at 11 μm over a period about 6 yr.

Adopting a distance of 1.74 ± 0.2 kpc (Massey & Thompson 1991), Schuster et al. (2009) estimated NML Cyg's minimum bolometric luminosity to be $3.15 \pm 0.74 \times 10^5$ $L_\odot$, which is similar to that of other red hypergiants and places it near the empirical upper-luminosity boundary in the Hertzsprung-Russell (H-R) diagram (Schuster et al. 2006). However, the estimated luminosity of a star depends on the square of its distance. Thus, an accurate distance is crucial to derive a reliable luminosity and the location on the H-R diagram. Recently, trigonometric parallaxes of circumstellar maser sources (H_2O or SiO) surrounding red hypergiants with VLBI phase-referencing have been measured with accuracies of 20–80 μas (Choi et al. 2008; Zhang et al. 2012; Asaki et al. 2010). We carried out a program to measure the trigonometric parallax and proper motion of masers in the circumstellar envelope (CSE) of NML Cyg with the National Radio Astronomical Observatory's[1] (NRAO's) Very Long Baseline Array (VLBA).

---

[1] The national Radio Astronomy Observatory is a facility of the National Science Foundation operated under cooperative agreement by Associated Universities, Inc.

In addition to distance, another fundamental stellar parameter is size. NML Cyg's high mass-loss rate results in a dense CSE, and the star is faint and hard to observe at visual wavelengths due to high extinction. However, it is extremely luminous in the infrared. Ridgway et al. (1986) used infrared speckle interferometric observations of NML Cyg and a simple model of multiple shells to derive an inner radius for its dust shell of 45 ± 12 mas. They also obtained the star's effective temperature, $T_{\mathrm{eff}} \approx 3250$ K, which is appropriate for an M6 III star (Johnson 1967). Monnier et al. (1997) conducted infrared interferometry at 11.15 μm, yielding evidence for multiple dust shells and asymmetric dust emission around NML Cyg. They obtained better fits to all data by assuming a $T_{\mathrm{eff}} \approx 2500$ K, using a model (Rowan-Robinson & Harris 1983). Blöcker et al. (2001) presented diffraction-limited 2.13 μm observations with 73 mas resolution and obtained a bolometric flux of $F_{\mathrm{bol}} = 3.63 \times 10^9$ W m^{-2}, corresponding to a stellar luminosity of $L_{\mathrm{bol}} = 1.13 \times 10^5 \times (d/\mathrm{kpc})^2$ $L_{\odot}$. Using the spectral energy distribution (SED) from 2 to 50 μm, they derived a stellar diameter of 16.2 mas assuming $T_{\mathrm{eff}} = 2500$ K. Clearly, a direct detection of the star would be complementary to the methods mentioned above. Radio continuum emission from the evolved star's photosphere can be imaged with the Very Large Array (VLA), using H_2O or SiO masers as a phase reference (Reid & Menten 1990, 1997, 2007; Zhang et al. 2012). Such observations allow us to directly measure the size of NML Cyg's radio photosphere and, using the observed flux density and our measured distance, its effective temperature.

2. Observations and data reduction

2.1. VLBA phase-referencing observations

We conducted VLBI phase-referencing observations of NML Cyg at 22 and 43 GHz with the VLBA under program BZ036 with 7-h tracks on 2008 May 25, August 13 and November 8, and 2009 January 27 and May 3. This sequence samples the peaks of the sinusoidal trigonometric parallax curve and has low correlation coefficients among the parallax and proper motion parameters. We observed several extragalactic radio sources as potential background references for parallax solutions. We alternated between two ≈ 16 min blocks at 22 and 43 GHz. Within a block, the observing sequence was NML Cyg, J2052+3635, NML Cyg, J2044+4005, NML Cyg, J2046+4106, NML Cyg, J2049+4118. We switched between the maser target and background sources every 40 s for 22 GHz and 30 s for 43 GHz, typically achieving 30 s for 22 GHz and 20 s for 43 GHz of on-source data.

We placed observations of two strong sources 3C 345 (J1642+3948) and 3C 454.3 (J2253+1608) near the beginning, middle, and end of the observations in order to monitor delay and electronic phase differences among the intermediate-frequency bands. The rapid-switching observations employed four adjacent bands of 8 MHz bandwidth and recorded both right and left circularly polarized signals. The H_2O and SiO masers were contained in the second band centered at a Local Standard of Rest (LSR) velocity of -7 km s^{-1}. In order to do atmospheric delay calibration, we placed "geodetic" blocks before and after our phase-reference observations. These data were taken in left circular polarization with eight 8 MHz bands that spanned 480 MHz of bandwidth between 22.0 and 22.5 GHz; the bands were spaced in a "minimum redundancy configuration" to uniformly sample, as best as possible, all frequency differences.
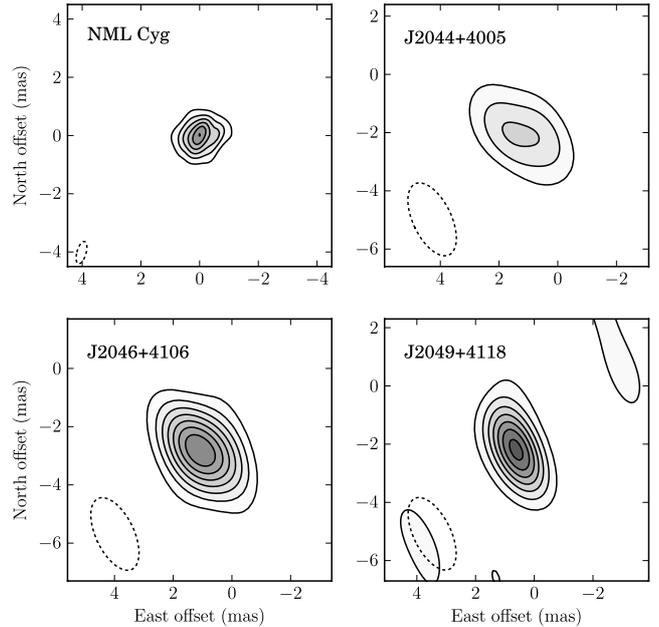
Fig. 1. Images of the H_2O maser reference spot and the extragalactic radio sources used for the parallax measurements of NML Cyg at the middle epoch (2008 November 08). Source names are in the upper left corner and the restoring beam (dotted ellipse) is in the lower left corner of each panel. Contour levels are spaced linearly at 3 Jy beam^{-1} for NML Cyg and 1.5 mJy beam^{-1} for the background sources.

The data were correlated in two passes with the VLBA correlator in Socorro, NM. One pass generated 16 spectral channels for all the data and a second pass generated 256 spectral channels, but only for the single (dual-polarized) frequency band containing the maser signals, giving a velocity resolution of 0.42 km s^{-1} for 22 GHz and 0.21 km s^{-1} for 43 GHz, respectively. Generally, the data calibration was performed with the NRAO Astronomical Image Processing System (AIPS), following similar procedures as described in Reid et al. (2009a). We used an H_2O maser spot at a V_{LSR} of 5.22 km s^{-1} and a SiO maser spot at a V_{LSR} of -5.70 km s^{-1} as phase-reference sources, because they are considerable stronger than the background source and could be detected on individual baselines in the available on-source time. We imaged the calibrated data with the AIPS task IMAGR; Fig. 1 shows example images at 22 GHz from the middle epoch. Table 1 lists the positions, intensities, source separations, LSR velocity of the reference maser spot and synthesized beam sizes.

2.2. VLA observation for radio photosphere

In addition to the VLBA observations, we carried out an observation of the radio photosphere and maser emission toward NML Cyg at 43 GHz with the VLA in its largest (A) configuration under program AZ178 on 2008 December 20. We used a dual intermediate frequency band setup in continuum mode with a narrow (3.125 MHz) band centered at V_{LSR} of -18 km s^{-1} for the $v = 1, J = 1 \rightarrow 0$ SiO maser line (rest frequency of 43 122.027 MHz) and a broad (50 MHz) band centered ≈ 50 MHz above in a line-free portion of the spectrum. Additionally, we observed the SiO maser emission in two subbands centered at V_{LSR} of -18 and -5 km s^{-1} at high spectral resolution (channel spacing of 97.6563 kHz and bandwidth of

B. Zhang et al.: Distance and size of NML Cyg

Table 1. Positions and brightnesses.

Source	RA (J2000) (h m s)	Dec (J2000) (° ′ ″)	S_p (Jy/beam)	θ_{sep} (°)	PA (°)	V_{LSR} (km s^{-1})	Beam (mas mas °)
(1)	(2)	(3)	(4)	(5)	(6)	(7)	(8)
22 GHz							
NML Cyg.......	20 46 25.5444	40 06 59.383	16–77	...	...	5.22	0.6 × 0.3 @ −08
J2052+3635....	20 52 52.0550	36 35 35.300	0.050	3.7	−19	...	2.7 × 1.4 @ +31
J2044+4005....	20 44 11.0877	40 05 36.360	0.005	0.4	+87	...	2.7 × 1.3 @ +25
J2046+4106....	20 46 21.8414	41 06 01.107	0.014	1.0	−01	...	2.7 × 1.2 @ +24
J2049+4118....	20 49 43.9548	41 18 14.583	0.011	1.3	+28	...	2.7 × 1.2 @ +26
43 GHz							
NML Cyg.......	20 46 25.5378	40 06 59.413	3.4	...	...	−5.70	0.3 × 0.1 @ −07
J2046+4106....	20 46 21.8414	41 06 01.107	0.017	1.0	−01	...	0.7 × 0.4 @ −25

Notes. The fourth and seventh columns give the peak brightnesses (S_p) and V_{LSR} of reference maser spot. The fifth and sixth columns give the separations (θ_{sep}) and position angles (PA) east of north of the background sources relative to the maser. The last column gives the FWHM size and PA of the Gaussian restoring beam. Calibrator J2052+3635 is from the VLBA Calibrator Survey (VCS) by Kovalev et al. (2007). The other calibrators are from the VLA program BZ035.
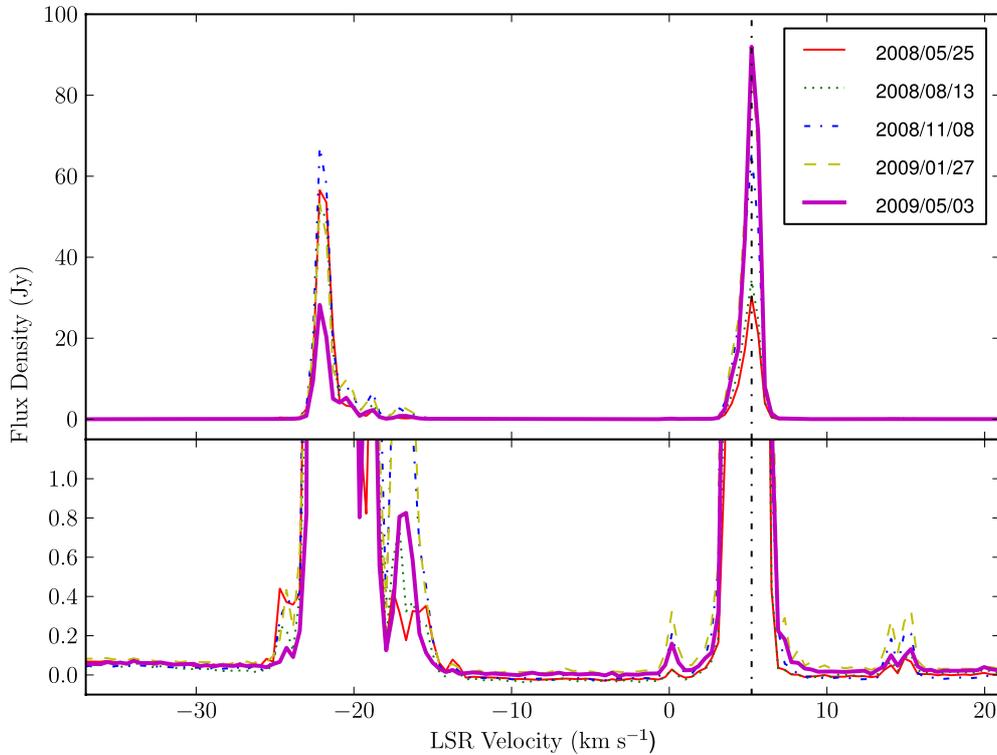
Fig. 2. Interferometer (scalar averaged cross-power amplitude over the full duration of the observation) spectra of the H$_2$O masers toward NML Cyg obtained with the inner 5 antennae of the VLBA at five epochs. The vertical dash-doted line indicates the maser feature at V_{LSR} of 5.22 km s^{-1} which served as the phase-reference. The *lower panel* shows a 100-times blow-up of the H$_2$O spectra shown in *upper panel*. (This figure is available in color in electronic form.)

6.25 MHz) with several scans in spectral-line mode interspersed among the dual-band continuum observations. We also observed H$_2$O maser emission (rest frequency of 22 235.080 MHz) centered at V_{LSR} of 5 km s^{-1} with a channel spacing of 48.8281 kHz and bandwidth of 6.25 MHz in a snapshot mode.

A typical observing unit for our continuum observations consisted of a ≈50 min NML Cyg scan, followed by a ≈5 min scan of, alternately, the quasar J2015+3710 and J2012+4628. For a spectral-line observation, we observed a calibrator for about 3 min and NML Cyg for 5 min. Absolute flux density calibration was established by an observation of 3C 286 (J1331+3030), assuming a flux density of 1.554 Jy at 43 GHz and 2.540 Jy at

22 GHz. Data calibration procedures are described in detail in Reid & Menten (1997, 2007).

3. Results

3.1. Maser spectrum and spatial distribution

Figure 2 shows scalar averaged cross-power spectra of H$_2$O maser emission observed using only the inner 5 antennae of the VLBA at all five epochs. The H$_2$O maser emission spans a V_{LSR} range from about −25 to 17 km s^{-1}, which is consistent with previous observations (Richards et al. 1996; Nagayama et al. 2008). One can see that the flux densities of some maser
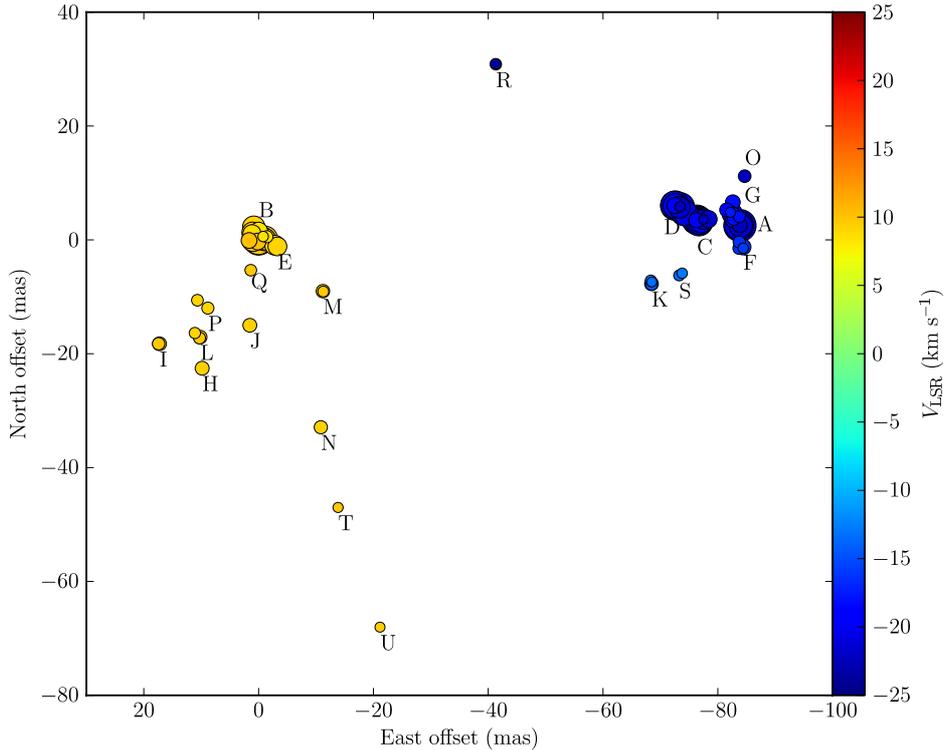
Fig. 3. Spatial distribution of the H$_2$O maser features toward NML Cyg from VLBA observations at five epochs. Each maser spot is represented by a letter label and a filed circle whose area is proportional to the logarithm of the flux density, using the position and flux density from the epoch at which it was first detected. The color bar denotes the $V_{\rm LSR}$ range from −25 to +25 km s^{-1}. The reference maser spot is in feature B, located at $(0,0)$ mas. (This figure is available in color in electronic form.)

features varied considerably from epoch to epoch within about 1.0 yr, while the peaks of blue-shifted ($V_{\rm LSR} = -22.17$ km s^{-1}) and red-shifted ($V_{\rm LSR} = 5.22$ km s^{-1}) features appear more stable. We confirmed that the brightest and most blue-shifted component appears to exhibit a velocity drift, the LSR velocities of this component in 1981, 1993, 2006 and 2008−2009 (this paper) were −18, −20, −21.8 and −22.2 km s^{-1}, the resulting acceleration is consistent with that derived by Shintani et al. (2008).

Figure 3 shows the spatial distribution of H$_2$O maser emission toward NML Cyg relative to the reference maser spot at $V_{\rm LSR} = 5.22$ km s^{-1} from observations at five epochs. We considered maser spots at different epochs as being from the same feature if their positions in the same spectral channel were coincident within x mas (where $x = 3$ mas yr^{-1} × Δt yr, and Δt is the time gap between two epochs), corresponding to a linear motion of less than 23 km s^{-1}. Selecting the bright maser spots with flux density >0.5 Jy beam^{-1} and $SNR > 10$ in each channel, we found 21 features that were detected at one or more epochs.

The total extent of the H$_2$O maser spot distribution is about 120 mas, which is consistent with previous studies from VLBI observations (Marvel 1996; Nagayama et al. 2008). Our first epoch observation took place about 1 yr later than the last epoch in Nagayama et al. (2008), and we found that the most redshifted maser cluster (including features B and E) and the most blue shifted maser cluster (including features D and C) in Fig. 3 are consistent with features at $V_{\rm LSR}$ about 6 and −22 km s^{-1} in Nagayama et al. (2008), respectively. These two dominant maser clusters are about 70 mas apart. This suggests that even though the spatial distribution changes in details, the maser features at the $V_{\rm LSR}$ near the distribution of the masers in the two peaks remains relatively stable.

Richards et al. (1996) reported an irregular ring of emission ≈200 mas across and a pair of outlying features to the northwest (NW) and south-east (SE), nearly 600 mas apart, based on MERLIN observations (Yates & Cohen 1994; Richards et al. 1996) and VLA observations (Johnston et al. 1985). The prominent maser features in the irregular ring are consistent with the features at $V_{\rm LSR}$ about 5 and −22 km s^{-1} reported in this paper. However, the NW and SE maser features were not detected in our VLBA nor in previous VLBI observations (Marvel 1996; Nagayama et al. 2008). For our VLBA observations, typical diameters of the H$_2$O maser spots are ≈1 mas and the detected limitation is ≈10 mJy. This corresponds to a brightness temperature lower limit of ≈4×10^7 K. However, the brightness temperatures for the two outlying features reported by Richards et al. (1996) are ≈10^7 K. This might be the reason why the outlying features were not detected with VLBI observations.

Unlike the H$_2$O maser, the SiO maser emission toward NML Cyg during our observation was very weak, and phase referencing with the maser succeeded only at the last epoch. Because we could register H$_2$O and SiO masers to the same background sources, the relative position between the reference maser spots for two maser species should be accurate to ±1 mas (see Fig. 4). The brightest SiO maser features detected in our observations are at $V_{\rm LSR}$ about −5.70 and 11.03 km s^{-1}. This differs from the VLBA observation of the same $v = 1, J = 1 \rightarrow 0$ SiO maser emission by Boboltz & Marvel (2000). The extent of the maser distribution is about 30 mas and is consistent with the diameter of the ring-like distribution from about 10 yr earlier. From a VLA observation of $v = 0, J = 1 \rightarrow 0$ SiO maser emission, Boboltz & Claussen (2004) reported a radius of ≈50 mas for the maser distribution, which is consistent with the inner boundary for the dust shell at 2.13 μm (Blöcker et al. 2001).
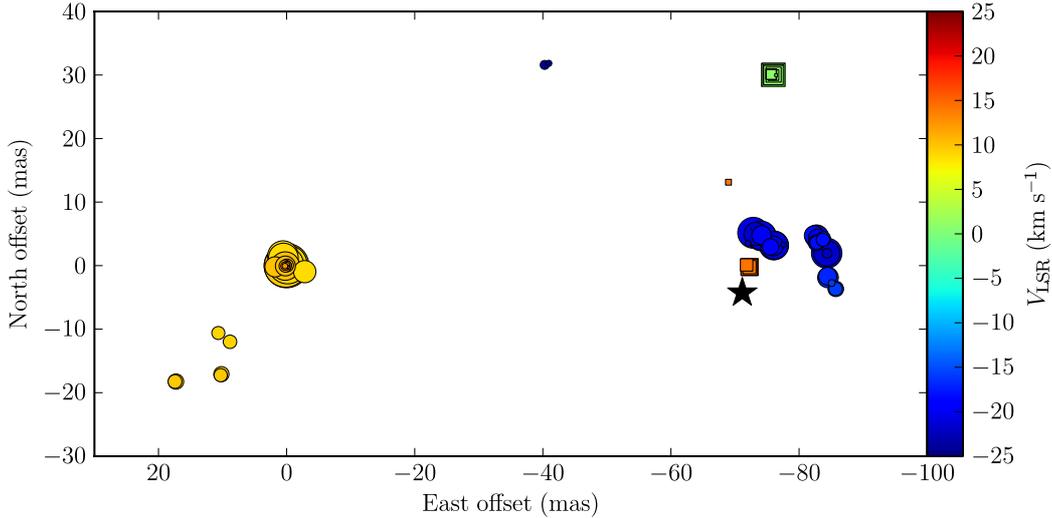
Fig. 4. Spatial distribution of the H_2O (circle) maser and SiO (square) maser spots toward NML Cyg from the fifth epoch observation. Each maser spot is represented by a filled circle or square whose area is proportional to the logarithm of the flux density. The position of the central star is indicated by a star (see the text in Sect. 3.3). The color bar denotes the V_{LSR} range from −25 to 25 km s^{-1} of the maser features. The reference H_2O maser spot is located at $(0, 0)$ mas. (This figure is available in color in electronic form.)

3.2. Parallax and proper motion

We fitted elliptical Gaussian brightness distributions to the images of strong maser spots and the extragalactic radio sources for all five epochs. The change in position of each maser spot relative to each background radio source was modeled by the parallax sinusoid in both coordinates (determined by a single parameter, the star's parallax) and a linear proper motion in each coordinate. The extragalactic source with the best known position, J2052+3635, was relatively far (3.7°) from NML Cyg, and it was only used to determine the absolute position of the maser reference spot. We used the other three calibrators, which are separated by less than 1.5° from NML Cyg, to determine the parallax.

As mentioned in Zhang et al. (2012), the apparent motions of the maser spots can be complicated by a combination of spectral blending and changes in intensity. Thus, for parallax fitting, one needs to find stable, unblended spots and/or use many maser spots to average out these effects. Thus, we first fitted a parallax and proper motion to the position offsets for each H_2O maser spot relative to each background source separately. In Fig. 5, we plot the position of the maser spot at $V_{LSR} = 6.48$ km s^{-1} (the first maser spot listed in Table 2) relative to the three background radio sources as an example, with superposed curves representing a model that uses a combined estimate for the parallax and proper motion as described below. This is one of the most redshifted compact and unblended spots that was detectable at all five epochs.

Table 2 shows the independently estimated parallaxes and proper motions for each maser spot and extragalactic source pair. While the parallaxes should be identical within measurement uncertainties, the proper motions are expected to vary among maser spots owing to internal motions of ≈15 km s^{-1} (1.9 mas yr^{-1} at a distance of 1.6 kpc). While most of the maser spot parallaxes show good internal consistency, the dispersion of parallax estimates over the entire ensemble is considerably larger than the formal errors would suggest. This is caused by residual systematic errors affecting the fits, which originate in the complexity and evolution of blended spectral and spatial structure for some of the masers.

Among these independent solutions, we found the parallaxes associated with maser spot at $V_{LSR} = -19.64$ km s^{-1} had the largest relative uncertainties of ≈200 μas. The spots in this feature are likely affected by line blended, and we discarded the data for this feature. We used all remaining position data in a combined solution, which used a single parallax parameter for all maser spots and extragalactic source pairs (but allowed for different proper motions for different maser spots).

The combined parallax estimate is 0.620 ± 0.047 mas, corresponding to a distance of $1.61^{+0.13}_{-0.11}$ kpc, placing NML Cyg possibly in a Local (Orion) arm. The quoted uncertainty is the formal error multiplied by $\sqrt{n}$ (where $n = 18$ is the number of maser spots used in the final parallax fit) to allow for the possibility of correlated position variations for all the maser spots. This could result from small variations in the background source or from un-modeled atmospheric delays, both of which would affect the maser spots nearly identically (Reid et al. 2009a). The un-weighted average absolute proper motion of all selected maser spots is $\mu_x = -1.55 \pm 0.42$ mas yr^{-1} and $\mu_y = -4.59 \pm 0.41$ mas yr^{-1}, where $\mu_x = \mu_\alpha \cos \delta$ and $\mu_y = \mu_\delta$.

Combining the parallax and proper motion measurements with the systemic V_{LSR} of -1.0 ± 2 km s^{-1} (Kemper et al. 2003; Etoka & Diamond 2004) enable us to determine the three-dimensional peculiar motion (relative to circular motion around the Galactic center) of NML Cyg. Adopting a flat rotation curve for the Milky Way with rotation speed of LSR $\Theta_0 = 239 \pm 7$ km s^{-1}, distance to the Galactic center of $R_0 = 8.3 \pm 0.23$ kpc (Brunthaler et al. 2011), and the solar motion of $(U_\odot = 11.1^{+0.69}_{-0.75}, V_\odot = 12.24^{+0.47}_{-0.47}, W_\odot = {}^{+0.37}_{-0.36})$ km s^{-1} from HIPPARCOS measurement revised by Schönrich et al. (2010), we estimate a peculiar motion for NML Cyg of $(U_s = -2.5 \pm 3.8, V_s = -6.1 \pm 2.1, W_s = -4.8 \pm 3.3)$ km s^{-1}, where U_s, V_s, W_s are directed toward the Galactic center, in the direction of Galactic rotation and toward the North Galactic Pole (NGP), respectively. Thus, NML Cyg is orbiting the Galaxy slower than expected from a circular orbit for a flat rotation curve, similarly to the average of many massive star forming regions found by Reid et al. (2009b). The peculiar velocity components toward the Galactic center and the NGP are relatively small with somewhat larger uncertainties.
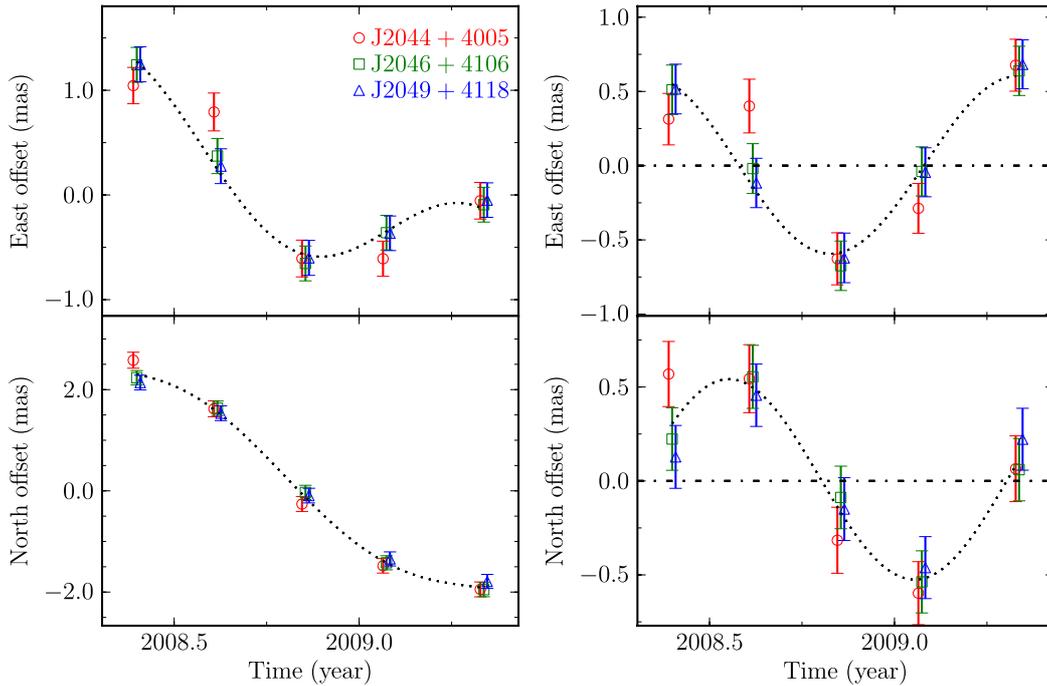
Table 2. Parallax and proper motion fits.

Source	Region	V_{LSR} (km s^{-1})	Parallax (mas)	μ_x (mas yr^{-1})	μ_y (mas yr^{-1})	Δx (mas)	Δy (mas)
J2044+4005	B	6.48	0.68 ± 0.10	−1.66 ± 0.58	−4.53 ± 0.19	−0.44 ± 0.19	2.19 ± 0.06
	B	6.06	0.72 ± 0.10	−1.70 ± 0.52	−4.33 ± 0.19	−0.37 ± 0.17	2.09 ± 0.05
	B	5.64	0.70 ± 0.09	−1.59 ± 0.48	−4.47 ± 0.18	−0.50 ± 0.16	2.18 ± 0.05
	B	5.22	0.70 ± 0.08	−1.68 ± 0.44	−4.55 ± 0.15	−0.63 ± 0.15	2.29 ± 0.04
	B	4.80	0.69 ± 0.06	−1.31 ± 0.47	−4.73 ± 0.12	−0.90 ± 0.16	2.55 ± 0.03
	B	4.37	0.55 ± 0.06	−1.85 ± 0.18	−5.50 ± 0.15	−0.66 ± 0.06	3.10 ± 0.04
	B	3.95	0.73 ± 0.07	−1.08 ± 0.52	−4.59 ± 0.14	−0.25 ± 0.17	3.80 ± 0.04
	F	−18.80	0.69 ± 0.10	−1.81 ± 0.43	−5.25 ± 0.20	−85.02 ± 0.14	0.71 ± 0.06
	F	−19.22	0.65 ± 0.12	−1.90 ± 0.39	−5.43 ± 0.25	−84.93 ± 0.13	0.94 ± 0.08
	F	−19.64	0.88 ± 0.21	−3.34 ± 0.93	−5.01 ± 0.41	−83.88 ± 0.31	6.87 ± 0.12
	G	−20.06	0.59 ± 0.12	−1.28 ± 0.33	−4.37 ± 0.32	−83.05 ± 0.11	6.98 ± 0.10
	A	−20.48	0.66 ± 0.09	−1.99 ± 0.36	−4.85 ± 0.18	−83.15 ± 0.12	6.99 ± 0.05
	A	−20.90	0.73 ± 0.10	−2.25 ± 0.45	−4.98 ± 0.19	−83.20 ± 0.15	6.96 ± 0.05
	A	−21.32	0.66 ± 0.09	−1.24 ± 0.33	−5.06 ± 0.20	−76.67 ± 0.11	5.59 ± 0.06
	A	−21.75	0.66 ± 0.10	−1.31 ± 0.32	−4.99 ± 0.22	−76.78 ± 0.11	5.63 ± 0.07
	A	−22.17	0.75 ± 0.07	−2.23 ± 0.62	−5.15 ± 0.14	−84.58 ± 0.20	4.52 ± 0.04
	A	−22.59	0.75 ± 0.08	−2.06 ± 0.54	−5.15 ± 0.14	−84.71 ± 0.18	4.50 ± 0.04
	A	−23.01	0.70 ± 0.09	−2.12 ± 0.42	−5.17 ± 0.17	−84.77 ± 0.14	4.46 ± 0.05
	R	−24.27	0.71 ± 0.06	−0.63 ± 0.53	−3.88 ± 0.12	−41.28 ± 0.18	33.57 ± 0.03
J2046+4106	B	6.48	0.63 ± 0.05	−1.56 ± 0.13	−4.29 ± 0.13	−0.23 ± 0.05	2.73 ± 0.04
	B	6.06	0.62 ± 0.01	−1.59 ± 0.02	−4.12 ± 0.16	−0.16 ± 0.01	2.64 ± 0.05
	B	5.64	0.64 ± 0.01	−1.50 ± 0.02	−4.24 ± 0.15	−0.29 ± 0.01	2.72 ± 0.05
	B	5.22	0.69 ± 0.01	−1.60 ± 0.02	−4.27 ± 0.17	−0.42 ± 0.01	2.83 ± 0.06
	B	4.80	0.61 ± 0.01	−1.21 ± 0.02	−4.53 ± 0.22	−0.68 ± 0.01	3.10 ± 0.07
	B	4.37	0.57 ± 0.09	−1.77 ± 0.26	−5.20 ± 0.22	−0.46 ± 0.09	3.64 ± 0.07
	B	3.95	0.56 ± 0.03	−0.96 ± 0.06	−4.46 ± 0.25	−0.02 ± 0.02	4.36 ± 0.08
	F	−18.80	0.62 ± 0.03	−1.72 ± 0.08	−5.03 ± 0.18	−84.81 ± 0.03	1.26 ± 0.06
	F	−19.22	0.64 ± 0.03	−1.82 ± 0.07	−5.14 ± 0.07	−84.73 ± 0.02	1.49 ± 0.02
	F	−19.64	0.81 ± 0.20	−3.24 ± 0.50	−4.77 ± 0.59	−83.67 ± 0.17	7.42 ± 0.19
	G	−20.06	0.61 ± 0.10	−1.21 ± 0.28	−4.04 ± 0.26	−82.85 ± 0.09	7.52 ± 0.08
	A	−20.48	0.65 ± 0.04	−1.91 ± 0.11	−4.57 ± 0.15	−82.94 ± 0.04	7.54 ± 0.05
	A	−20.90	0.67 ± 0.02	−2.15 ± 0.04	−4.75 ± 0.17	−82.99 ± 0.02	7.51 ± 0.06
	A	−21.32	0.64 ± 0.04	−1.16 ± 0.10	−4.78 ± 0.21	−76.47 ± 0.03	6.14 ± 0.07
	A	−21.75	0.64 ± 0.05	−1.23 ± 0.11	−4.71 ± 0.19	−76.57 ± 0.04	6.17 ± 0.06
	A	−22.17	0.53 ± 0.01	−2.10 ± 0.02	−5.07 ± 0.20	−84.34 ± 0.01	5.08 ± 0.06
	A	−22.59	0.58 ± 0.01	−1.95 ± 0.02	−5.02 ± 0.18	−84.48 ± 0.01	5.05 ± 0.06
	A	−23.01	0.63 ± 0.09	−2.03 ± 0.38	−4.94 ± 0.17	−84.56 ± 0.13	5.01 ± 0.05
	R	−24.27	0.54 ± 0.02	−0.52 ± 0.05	−3.75 ± 0.28	−41.05 ± 0.02	34.13 ± 0.09
J2049+4118	B	6.48	0.62 ± 0.02	−1.48 ± 0.07	−4.03 ± 0.05	0.13 ± 0.02	2.15 ± 0.02
	B	6.06	0.63 ± 0.03	−1.52 ± 0.08	−3.82 ± 0.13	0.20 ± 0.03	2.05 ± 0.04
	B	5.64	0.64 ± 0.04	−1.42 ± 0.10	−3.95 ± 0.12	0.07 ± 0.03	2.13 ± 0.04
	B	5.22	0.68 ± 0.05	−1.52 ± 0.11	−3.99 ± 0.16	−0.06 ± 0.04	2.24 ± 0.05
	B	4.80	0.62 ± 0.04	−1.14 ± 0.09	−4.23 ± 0.18	−0.33 ± 0.03	2.51 ± 0.06
	B	4.37	0.52 ± 0.07	−1.68 ± 0.35	−4.95 ± 0.14	−0.09 ± 0.11	3.06 ± 0.04
	B	3.95	0.59 ± 0.06	−0.89 ± 0.15	−4.14 ± 0.19	0.33 ± 0.05	3.77 ± 0.06
	F	−18.80	0.64 ± 0.06	−1.64 ± 0.17	−4.72 ± 0.13	−84.45 ± 0.06	0.67 ± 0.04
	F	−19.22	0.62 ± 0.01	−1.73 ± 0.13	−4.86 ± 0.03	−84.37 ± 0.04	0.90 ± 0.01
	F	−19.64	0.81 ± 0.17	−3.17 ± 0.42	−4.47 ± 0.53	−83.31 ± 0.14	6.83 ± 0.17
	G	−20.06	0.62 ± 0.10	−1.13 ± 0.27	−3.74 ± 0.26	−82.49 ± 0.09	6.93 ± 0.08
	A	−20.48	0.62 ± 0.04	−1.83 ± 0.16	−4.32 ± 0.08	−82.58 ± 0.05	6.95 ± 0.02
	A	−20.90	0.67 ± 0.04	−2.08 ± 0.10	−4.45 ± 0.12	−82.63 ± 0.03	6.92 ± 0.04
	A	−21.32	0.64 ± 0.06	−1.08 ± 0.15	−4.49 ± 0.15	−76.11 ± 0.05	5.55 ± 0.05
	A	−21.75	0.65 ± 0.06	−1.15 ± 0.17	−4.41 ± 0.14	−76.21 ± 0.06	5.58 ± 0.04
	A	−22.17	0.55 ± 0.05	−2.03 ± 0.11	−4.76 ± 0.21	−83.99 ± 0.04	4.49 ± 0.07
	A	−22.59	0.60 ± 0.05	−1.87 ± 0.10	−4.70 ± 0.18	−84.13 ± 0.04	4.46 ± 0.06
	A	−23.01	0.65 ± 0.05	−1.95 ± 0.47	−4.64 ± 0.09	−84.20 ± 0.15	4.42 ± 0.03
	R	−24.27	0.56 ± 0.06	−0.44 ± 0.13	−3.44 ± 0.22	−40.70 ± 0.05	33.54 ± 0.07

Table 2. continued.

Source	Region	$V_{\rm LSR}$ (km s^{-1})	Parallax (mas)	μ_x (mas yr^{-1})	μ_y (mas yr^{-1})	Δx (mas)	Δy (mas)
Combined							
	B	6.48		-1.56 ± 0.13	-4.29 ± 0.11		
	B	6.06		-1.59 ± 0.13	-4.11 ± 0.11		
	B	5.64		-1.49 ± 0.13	-4.24 ± 0.11		
	B	5.22		-1.58 ± 0.13	-4.33 ± 0.11		
	B	4.80		-1.21 ± 0.13	-4.50 ± 0.11		
	B	4.37		-1.78 ± 0.13	-5.14 ± 0.11		
	B	3.95		-0.97 ± 0.13	-4.39 ± 0.11		
	F	-18.80		-1.71 ± 0.13	-5.02 ± 0.11		
	F	-19.22		-1.81 ± 0.13	-5.14 ± 0.11		
	G	-20.06		-1.21 ± 0.13	-4.02 ± 0.11		
	A	-20.48		-1.90 ± 0.13	-4.59 ± 0.11		
	A	-20.90		-2.14 ± 0.13	-4.78 ± 0.11		
	A	-21.32		-1.15 ± 0.13	-4.79 ± 0.11		
	A	-21.75		-1.22 ± 0.13	-4.71 ± 0.11		
	A	-22.17		-2.11 ± 0.13	-4.98 ± 0.11		
	A	-22.59		-1.95 ± 0.13	-4.97 ± 0.11		
	A	-23.01		-2.03 ± 0.13	-4.94 ± 0.11		
	R	-24.27		-0.53 ± 0.13	-3.66 ± 0.11		
			0.620 ± 0.047				

Notes. Absolute proper motions are defined as $\mu_x = \mu_{\alpha\cos\delta}$ and $\mu_y = \mu_\delta$.


Fig. 5. Parallax and proper motion data (markers) and a best-fitting model (dotted lines) that uses a combined estimate for the parallax and proper motion for the maser spot at the $V_{\rm LSR}$ of 6.48 km s^{-1}. Plotted are positions of the maser spot relative to the extragalactic radio sources J2044+4005 (circles), J2046+4106 (squares) and J2049+4118 (triangles). *Left panel*: eastward (*upper panel*) and northward (*lower panel*) offsets versus time. *Right panel*: same as the *left panel*, except the best-fitting proper motion has been removed, displaying only the parallax signature. (This figure is available in color in electronic form.)

3.3. Radio photosphere and circumstellar maser emission from VLA observation

We detected the radio photosphere of NML Cyg at 43 GHz and made a uniformly weighted image (see Fig. 7). We also fitted a model of an uniformly bright disk to the uv-data directly using the AIPS task OMFIT, obtained a diameter of 44 ± 16 mas and integrated flux density of 0.82 ± 0.11 mJy. We binned the data and plotted the real part of the visibility versus baseline length in Fig. 6.

Taking the crude characteristics of the radio photosphere to be $R_{\rm rp} \approx 2 \times R_{\rm op}$, and $T_{\rm rp} \approx 0.71 \times T_{\rm op}$, which are inferred from the imaging of variable stars by Reid & Menten (1997) (where $R_{\rm rp}$ and $R_{\rm op}$ are the radii of the radio and optical
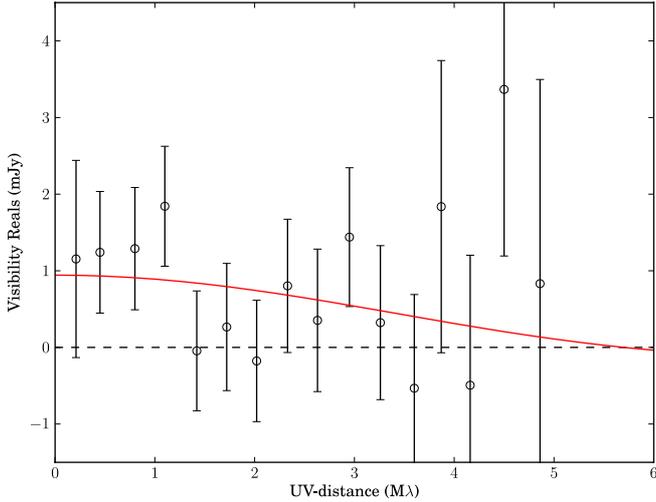
Fig. 6. Fringe visibility vs. baseline length measured for NML Cyg at 43 GHz on 2008 December 20 under VLA program AZ178. The solid line indicates a uniformly bright circular disk model with diameter of 44 mas.

photospheres, respectively, and $T_{\rm rp}$ and $T_{\rm op}$ are the effective temperatures of the radio and optical photospheres), the semi-diameter of radio photosphere, 22 mas, is reasonably consistent with that of 16.2 mas derived by Blöcker et al. (2001).

In order to register the SiO masers relative to the radio photosphere, we first measured the position of the radio photosphere from the broad-band data relative the maser emission from the narrow-band data. Next, we aligned the maser emission from the spectral-line data by producing a map of pseudo-continuum data by integrating the line data over the entire narrow-band. Because the narrow-band and the pseudo-continuum data cover the maser emission from the same velocity range, we can align them by comparing the positions of peaks in each map. This allows the positions of the emission in individual channels to be registered to the map of narrow-band data, and then to the radio photosphere. We estimated a position offset of the weak continuum source (radio photosphere) relative to the reference maser spot to be ($\Delta x = -8$, $\Delta y = -8$) mas with an uncertainty of ≈ 3 mas. Figure 7 shows the relative positions of the SiO maser and 43 GHz continuum emission used to register the images.

The relative offsets of the peaks of SiO maser emission and the central star agree well with observations of Mira variable stars (Reid & Menten 2007), which show the SiO maser emission surrounds the central star in a partial ring with radii of 2–3 $R_{\rm op}$. For NML Cyg the SiO radius is also consistent with the dust inner-radius of 45 mas (Ridgway et al. 1986).

In order to estimate the absolute position of the radio photosphere (which should be that of the central star), we have to align the SiO maser spots measured with the VLA with those from the VLBA observations. As discussed in Zhang et al. (2012), if a single spectral channel contains emission from across the source, the VLA position would be falsely interpreted as being near the center of the distribution. Furthermore, the VLBA observing date of SiO emission is about five months later than that of VLA. So, there is no guarantee that the VLA and VLBA maps should be identical. However, we found that the two maser clusters at $V_{\rm LSR}$ about 11 and -6 km s^{-1} in the VLBA map are in good agreement with those at similar $V_{\rm LSR}$ values in the VLA map, after shifted the VLBA map ($\Delta x = -13$, $\Delta y = 26$) mas, with an uncertainty of ≈ 5 mas. Thus, we can register the radio photosphere

to the VLBA SiO maser spots with a conservative uncertainty of 10 mas (see Fig. 8).

The absolute position of the reference SiO maser spot can be estimated relative to the extragalactic sources, yielding the absolute stellar position of NML Cyg at epoch 2008.868 of $\alpha_{\rm J2000} = 20^{\rm h}46^{\rm m}25{.}^{\rm s}5382 \pm 0{.}^{\rm s}0010$, $\delta_{\rm J2000} = 40°06'59{.}''379 \pm 0{.}''015$. The absolute position is consistent with, but considerably more accurate than, that from the Two Micron All Sky Survey (2MASS) by Skrutskie et al. (2006) (after converting to J2000 coordinates and accounting for our measured absolute proper motion); differences of 39 mas in right ascension and 10 mas in declination are well within the 170 mas uncertainty of the 2MASS position.

Figure 9 shows the H$_2$O maser distribution from our VLA observation. Similar to the map as shown in Fig. 3, the maser distribution is dominated by two maser clusters with a separation of ≈ 70 mas. However, the total extent of the maser distribution is much larger than that of VLBA map. The outlying maser spot to the south-east in the VLA map is likely associated with a feature reported by Richards et al. (1996).

4. Discussion

4.1. Relation to the Cyg region and OB association

Habing et al. (1982) observed a H II region located northwest of NML Cyg, and Morris & Jura (1983) suggested that it represented a portion of NML Cyg's CSE photoionized by the luminous and hot stars in the Cyg OB2 association. Cyg OB2 lies near the center of the X-ray emitting Cygnus X super bubble, which is composed of numerous individual H II regions, a number of Wolf-Rayet and O3 stars and several OB associations.

Recently, Rygl et al. (2012) reported distances from trigonometric parallax measurements of four 6.7 GHz methanol maser sources in the Cygnus X region that are consistent with 1.40 ± 0.08 kpc for this region (see Fig. 11). This is similar to the distance of 1.45 kpc to Cyg OB2 obtained by Hanson (2003), based on fitting 35 dwarf cluster members with spectral types between O7.5 and B1 to a 2×10^6 yr isochrone, and also consistent with latest estimated photometric distance of 1.5 kpc determined by Kharchenko et al. (2005), although slightly smaller than previous work quoting 1.74 kpc (Massey & Thompson 1991).

Given that the Cygnus X region contains huge amounts of dust, one might expect that this dust would extinguish the optical light from Cyg OB2. However, little extinction toward Cyg OB2 was found from the NIR extinction map of the region (Motte et al. 2007). We also note that the interstellar medium (ISM) absorption signatures from NML Cyg, seen in *Herschel* spectra of the H$_2$O ortho ($1_{1,0} \rightarrow 1_{0,1}$) and para ground-state ($1_{1,0} \rightarrow 0_{0,0}$) line (Teyssier et al. in prep.) and low-J CO transitions (Kemper et al. 2003), suggest that they arise from a cold gas component. One possible explanation is that the diffuse gas in Cygnus X is located in front of NML Cyg. Taking our distance of $1.61^{+0.13}_{-0.11}$ kpc to NML Cyg, we offer new observational evidence that NML Cyg might be associated with Cyg OB2.

As listed in Table 4, our measured absolute proper motion of NML Cyg is in good agreement with that of Cyg OB2, computed by averaging proper motions of the most probable cluster members (Kharchenko et al. 2005). NML Cyg's $V_{\rm LSR}$ of -1 ± 2 km s^{-1} is consist with the systemic $V_{\rm LSR}$ of 7 km s^{-1} (helio-centric velocity -10.3 km s^{-1}), within a dispersion of 6 km s^{-1}, for Cyg OB2 as estimated by Kiminki et al. (2007, 2008). For comparison, Table 4 also lists parameters for two other red hypergiants and their associated clusters. We find that
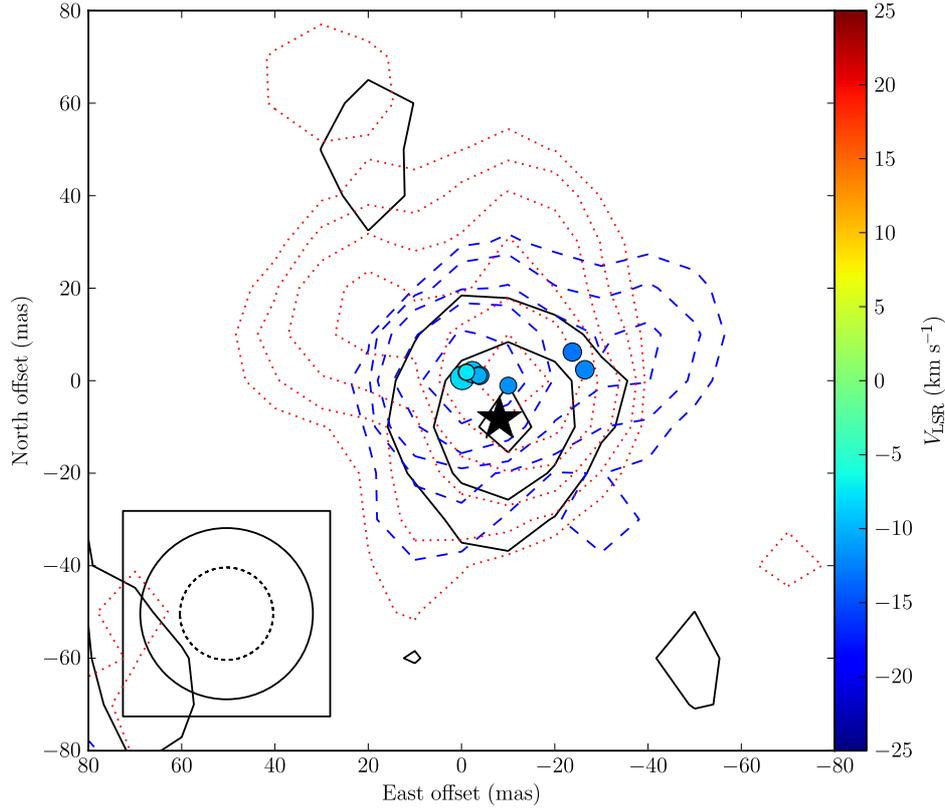
Fig. 7. SiO maser emissions integrated over V_{LSR} from -28.86 to -7.14 km s^{-1} (dashed contour) which is within the same V_{LSR} range as that of the narrow-band data, and V_{LSR} from -7.14 to 22.93 km s^{-1} (dotted contour) toward NML Cyg superposed on the 43 GHz continuum emission (solid contour) with peak position indicated by the star. The maser spots within the same V_{LSR} range as the narrow-band data are marked with circles, with size proportional to the logarithm of their flux densities. The V_{LSR} of the maser spots is color-coded as indicated by the color bar on the right side, which use the same range of V_{LSR} as other maser spots figures in this paper for comparison. All offsets are relative to the strongest maser emission at V_{LSR} of -4.66 km s^{-1}. The relative positions of the SiO maser and radio continuum emission is estimated to be accurate to ≈ 3 mas. Contour levels for integrated maser emission are 0.18 Jy beam^{-1} $\times$ 2^n, $n = 0 \ldots 5$ and for the radio continuum are integer multiples of 0.10 mJy beam^{-1}. The restoring beam for the maser (dotted circle) and continuum (solid circle) emissions are indicated in the lower left corner. (This figure is available in color in electronic form.)

**Table 4.** Comparison of astrometric parameters of red hypergiants and its associated clusters.

Star	Cluster	Separation (°)	Distance (pc)	μ_x (mas yr^{-1})	μ_y (mas yr^{-1})	V_{LSR} (km s^{-1})
(1)	(2)	(3)	(4)	(5)	(6)	(7)
NML Cyg			1610 ± 120	-1.55 ± 0.42	-4.59 ± 0.41	-01.0
	Cyg OB2	2.7	1500	-1.22 ± 0.20	-4.72 ± 0.24	$+07.0 \pm 6.0$
VY CMa			1200 ± 120	-2.80 ± 0.20	$+2.60 \pm 0.20$	$+22.0$
	NGC2362	1.3	1389	-2.03 ± 0.31	$+2.47 \pm 0.34$	$+06.2 \pm 8.9$
S Per			2400 ± 100	-0.49 ± 0.23	-1.19 ± 0.20	-38.5
	h Per	1.5	2079	-0.27 ± 0.26	-0.90 ± 0.39	-35.7 ± 2.0
	χ Per	1.5	2345	-0.46 ± 0.24	-0.23 ± 0.50	-35.8 ± 7.1

Notes. The first and second columns list the names of a red hypergiant and its associated cluster. The third column lists the separation between a star and the center of the cluster. The fourth to seventh columns list distance, proper motion eastward and northward and LSR velocity of red hypergiant or cluster. Parameters for NML Cyg are from this paper; parameters for VY CMa are from Zhang et al. (2012), except that V_{LSR} is from Menten et al. (2006); Parameters for S Per are from Asaki et al. (2010). Parameters for clusters are from Kharchenko et al. (2005), except that V_{LSR} of Cyg OB2 is from Kiminki et al. (2007, 2008).

the radio proper motions of stars and the optical proper motion of their associated clusters are in good agreement, providing new observational evidence for their association.

Figure 11 shows the positions of maser sources in the Cygnus X region with accurate parallax measurements and their peculiar motions projected on the sky. We find that the methanol sources are moving upward (toward increasing Galactic latitude) while NML Cyg and Cyg OB2 are moving downward from the Galactic plane. This suggest that the space motions in the Cygnus X region are much more complicated than expected from an expanding Strömgren sphere centered on Cyg OB2 with an angular diameter of 4° (Knödlseder 2003).
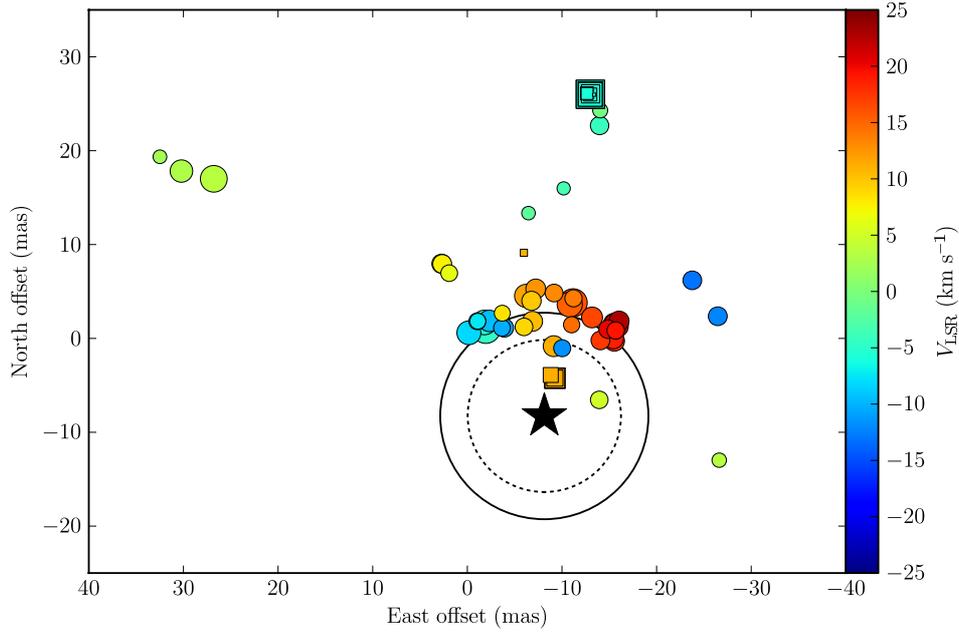
Fig. 8. Comparison of SiO maser distribution from the VLBA observation (squares) on 2009 May 25 and VLA observation (circles) on 2008 December 20, after cross-registration (see the text). The sizes of the markers are proportional to the logarithm of their flux densities. The V_{LSR} of the maser spots is color-coded as indicated by the color bar on the right side. The position of the central star is indicated as the star. The solid circle and dotted circle denote the stellar diameter of 22 mas from this paper and 16 mas from Blöcker et al. (2001), respectively. (This figure is available in color in electronic form.)
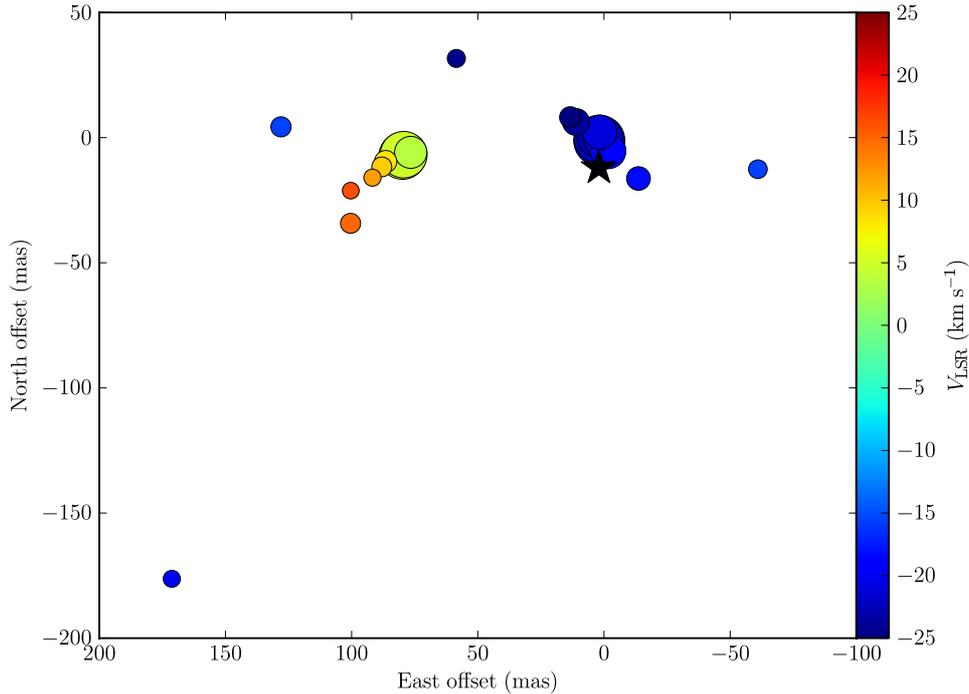

Fig. 9. H_2O maser emissions distribution toward NML Cyg from VLA observation on 2008 December 20. All offsets are relative to the strongest maser emission at V_{LSR} of -22.25 km s^{-1}. All the maser spots are marked with circles, with sizes proportional to the logarithm of their flux densities. The position of the central star is indicated by a star. (This figure is available in color in electronic form.)

4.2. Stellar parameters

Schuster et al. (2009) determined NML Cyg's minimum bolometric luminosity, $L_{bol} = (1.04 \pm 0.05) \times 10^5 \, (d/\text{kpc})^2 \, L_\odot$, by integrating its SED from 0.5 to 100 μm without correction for extinction. This luminosity is in good agreement with the estimate of $L_{bol} = 1.13 \times 10^5 \, (d/\text{kpc})^2 \, L_\odot$ by Blöcker et al. (2001). Adopting our measured distance of $1.61^{+0.13}_{-0.11}$ kpc, we

find NML Cyg's luminosity to be $(2.7 \pm 0.5) \times 10^5 \, L_\odot$. We note that a stellar temperature of 2500 K, first derived from a model by Rowan-Robinson & Harris (1983), gives a good fit to the infrared data (Monnier et al. 1997), as compared to a temperature of 3250 K obtained from spectroscopy by Ridgway et al. (1986).

To examine the evolutionary status of NML Cyg, we compared its position on the H-R diagram with stellar evolutionary
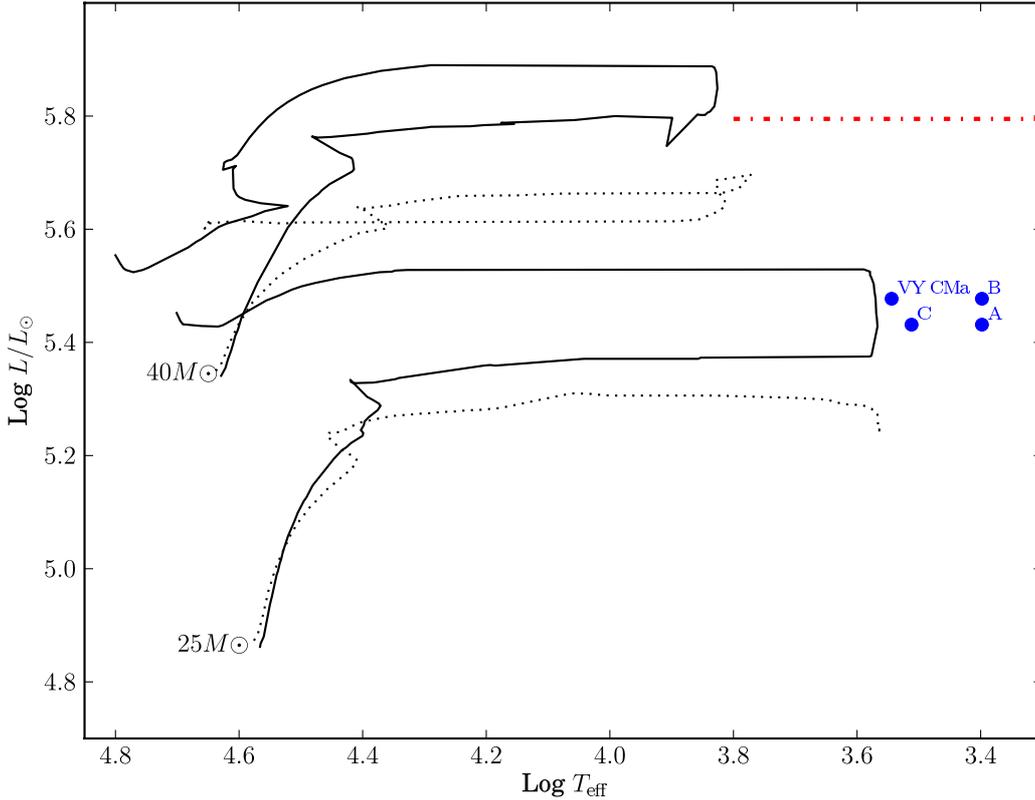
Fig. 10. Evolutionary tracks of 25 and 40 $M_\odot$ non-rotating (dotted lines) and rotating (solid lines) with a velocity of 300 km s^{-1}. The model assumes a star with near solar metallicity ($Z = 0.02$) evolving from the zero-age main sequence to the red supergiant and then Wolf-Rayet star phase. The dot-dashed line denotes the empirical upper luminosity boundary (for $T_{\rm eff}$ less than 6000 K) from Schuster et al. (2006). The filled circle labeled "VY CMa" represents the results for that star from Choi et al. (2008). For NML Cyg the filled circle labeled "A" corresponds to $T_{\rm eff}$ = 2500 K (Rowan-Robinson & Harris 1983; Monnier et al. 1997; Zubko et al. 2004) and 2.7×10^5 $L_\odot$ revised with the distance in this paper; filled circles "B" and "C" are for $T_{\rm eff}$ = 2500 K and 3.0×10^5 $L_\odot$ (Schuster et al. 2009) and $T_{\rm eff}$ = 3250 K (Ridgway et al. 1986) and 2.7×10^5 $L_\odot$.

tracks (Meynet & Maeder 2003), using different $T_{\rm eff}$ and luminosity values (see Fig. 10). Although NML Cyg's position with $T_{\rm eff}$ of 3250 K is more consistent with the evolutionary track than those with $T_{\rm eff}$ of 2500 K (compare dots "C" with "A"), we find that NML Cyg's position is closest to the evolutionary track with an initial mass of 25 $M_\odot$, instead of 40 $M_\odot$ quoted in Schuster et al. (2009), no matter which luminosity and $T_{\rm eff}$ we adopted (see dots "A", "B" and "C" in Fig. 10). This mass is similar to that of VY CMa, another red hypergiant star, estimated by Choi et al. (2008). Re-scaling NML Cyg's luminosity (compare dots "A" with "B") with our distance drops it in the H-R diagram well below the empirical upper luminosity boundary (see the red dot-dashed line in Fig. 10), which is not sensitive to temperature for stars <6000 K. However, NML Cyg's position on the H-R diagram, compared with the evolutionary track, constrains its age (by adopting the evolutionary time of the closest point to NML Cyg on the track) to be ≈8 Myr, which is considerably greater than that of ≈2–3 Myr for Cyg OB2 (Massey et al. 2001; Hanson 2003). Since the observational evidence now confirms that NML Cyg is associated with Cyg OB2, they are probably about the same age. If so, the stellar evolutionary model cannot be appropriate for NML Cyg.

NML Cyg's stellar size of 16.2 mas from Blöcker et al. (2001) was derived using the Stepan-Boltzmann law, adopting $T_{\rm eff}$ = 2500 K and a distance of 1.74 kpc. Rescaling this stellar diameter with our distance of 1.61 kpc gives 15.0 mas. For the radio photosphere, we fitted a round-disk model with a diameter of 44 ± 16 mas and flux density of 0.8 ± 0.1 mJy using the AIPS task OMFIT, and we calculate a (Rayleigh-Jeans) $T_{\rm eff}$ between 100 K and 6000 K (i.e., ±2σ). Clearly more observations are needed to improve this temperature constraint.

4.3. Maser distribution relative to radio photosphere

Richards et al. (1996) proposed a bipolar H_2O maser outflow and suggested the central star is located close to the prominent H_2O maser cluster at $V_{\rm LSR}$ about −22 km s^{-1} in the irregular ring, assuming the NW and SE feature lie approximately symmetrically about the star. Based on high-resolution HST observations, Schuster et al. (2006) find that the circumstellar material of NML Cyg shows an "arc-like" shape with a line of symmetry and an axis facing toward Cyg OB2, which is coincident with the H_2O maser (Richards et al. 1996) and ground state SiO distribution (Boboltz & Claussen 2004) around NML Cyg. They assumed the star is near the peak intensity in the optical images and coincident with the position of the strongest H_2O maser feature, then the maser shows an one-sided distribution within NML Cyg's nebula. This led to the suggestions that the masers are protected by the star's envelope from Cyg OB2's radiation and the arc-like shape of circumstellar material is the result of the interaction between the molecular outflow from NML Cyg and the near-UV continuum flux from Cyg OB2 (Schuster et al. 2009). Nagayama et al. (2008) presented three-dimensional kinematic data for H_2O maser features from multi-epoch VLBI observations and suggested an expanding outflow with the central star at the dynamical center.

However, after registering the radio photosphere to the SiO maser and then to the H_2O maser, we find that both the
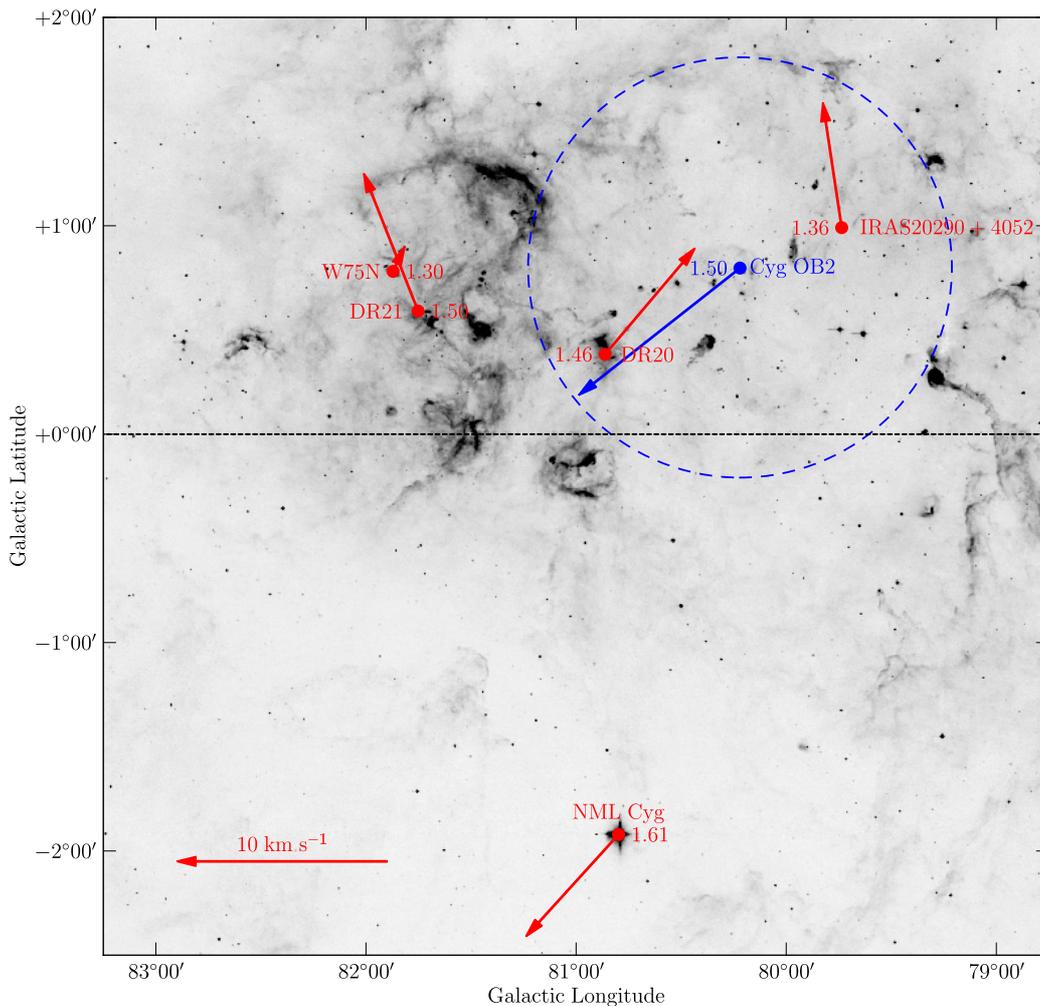
Fig. 11. Midcourse Space eXperiment (MSX) 8 μm image of the Cygnus X region overlaid with the peculiar motions for maser sources with parallax and proper motion measurements. The dotted line indicates the Galactic plane. The *dots* mark the water maser (NML Cyg, this paper) and the methanol maser sources (Rygl et al. 2012) and the center of Cyg OB2 (Kharchenko et al. 2005), with their distances labeled in kpc. The peculiar motions of sources are indicated with arrows. The approximate size of the Cyg OB2 association is denoted by a circle with diameter of 2° (Knödlseder 2000) (This figure is available in color in electronic form.)

SiO maser and H_2O maser are highly asymmetrically distributed around the NML Cyg's central star, which is located at southwest side of both the H_2O and SiO maser distribution, and there are H_2O and SiO masers located north-west of the central star. This is inconsistent with the model suggested by Schuster et al. (2006, 2009) based on the one-side H_2O maser distribution, since there are no masers located north-west of the central star. And the central star is not near the center of the two prominent maser clusters at V_{LSR} of about −22 and 5 km s^{-1} as Nagayama et al. (2008) suggested, but is closer to the maser cluster at V_{LSR} of about −22 km s^{-1}, which is coincident with that suggested by Richards et al. (1996). Considering that kinematic models for maser features are highly dependent on maser positions and motions respective to the central star, our direct determination of positions relative to the central star presents a crucial constraint for understanding the properties of the circumstellar material surrounding NML Cyg.

the circumstellar H_2O and SiO masers. Both the distance and proper motion of NML Cyg are consistent with those of the Cyg OB2 association within their joint uncertainties, confirming that NML Cyg is associated with Cyg OB2. We revised the stellar luminosity using the accurate distance from a trigonometric parallax measurement, suggesting that the location of NML Cyg on the HR diagram is consistent with the evolutionary track of an evolved star with an initial mass of 25 $M_\odot$. However, the derived age of 8 Myr for NML Cyg from the evolutionary track is much larger than that 2–3 Myr of Cyg OB2, suggesting that the evolutionary track might not be appropriate to NML Cyg.

After registering the radio photosphere to the H_2O and SiO maser, we find the central star is located close to a prominent H_2O maser cluster toward the north-west edge of the maser distribution. This is inconsistent with the model that the masers are off to one-side of the star and also the model for an expanding outflow with the star in the middle of two prominent H_2O maser clusters as previously suggested.

5. Conclusions

We have measured the trigonometric parallax and proper motion of NML Cyg from multiple epoch VLBA observations of

References

Abbott, D. C., Bieging, J. H., & Churchwell, E. 1981, ApJ, 250, 645
Asaki, Y., Deguchi, S., Imai, H., et al. 2010, ApJ, 721, 267
Blöcker, T., Balega, Y., Hofmann, K.-H., & Weigelt, G. 2001, A&A, 369, 142
Boboltz, D. A., & Claussen, M. J. 2004, ApJ, 608, 480
Boboltz, D. A., & Marvel, K. B. 2000, ApJ, 545, L149
Brunthaler, A., Reid, M. J., Menten, K. M., et al. 2011, Astron. Nachr., 332, 461
Choi, Y. K., Hirota, T., Honma, M., et al. 2008, PASJ, 60, 1007
Danchi, W. C., Green, W. H., Hale, D. D. S., et al. 2001, ApJ, 555, 405
Denisenkova, S. N., Larionova, L. V., & Khozov, G. V. 1988, Perem. Zvezdy, 22, 882
Etoka, S., & Diamond, P. 2004, MNRAS, 348, 34
Habing, H. J., Goss, W. M., & Winnberg, A. 1982, A&A, 108, 412
Hanson, M. M. 2003, ApJ, 597, 957
Johnson, H. L. 1967, ApJ, 149, 345
Johnson, H. L., & Morgan, W. W. 1954, ApJ, 119, 344
Johnston, K. J., Spencer, J. H., & Bowers, P. F. 1985, ApJ, 290, 660
Kemper, F., Stark, R., Justtanont, K., et al. 2003, A&A, 407, 609
Kharchenko, N. V., Piskunov, A. E., Röser, S., Schilbach, E., & Scholz, R.-D. 2005, A&A, 438, 1163
Kiminki, D. C., Kobulnicky, H. A., Kinemuchi, K., et al. 2007, ApJ, 664, 1102
Kiminki, D. C., Kobulnicky, H. A., Kinemuchi, K., et al. 2008, ApJ, 681, 735
Knödlseder, J. 2000, A&A, 360, 539
Knödlseder, J. 2003, in A Massive Star Odyssey: From Main Sequence to Supernova, eds. K. van der Hucht, A. Herrero, & C. Esteban, IAU Symp., 212, 505
Kovalev, Y. Y., Petrov, L., Fomalont, E. B., & Gordon, D. 2007, AJ, 133, 1236
Marvel, K. B. 1996, Ph.D. Thesis, New Mexico State Univ.
Massey, P., & Thompson, A. B. 1991, AJ, 101, 1408
Massey, P., DeGioia-Eastwood, K., & Waterhouse, E. 2001, AJ, 121, 1050
Menten, K. M., Philipp, S. D., Güsten, R., et al. 2006, A&A, 454, L107
Meynet, G., & Maeder, A. 2003, A&A, 404, 975
Monnier, J. D., Bester, M., Danchi, W. C., et al. 1997, ApJ, 481, 420
Morris, M., & Jura, M. 1983, ApJ, 267, 179
Motte, F., Bontemps, S., Schilke, P., et al. 2007, A&A, 476, 1243
Nagayama, T., Takeda, K., Omodaka, T., et al. 2008, PASJ, 60, 1069
Reddish, V. C., Lawrence, L. C., & Pratt, N. M. 1966, Publications of the Royal Observatory of Edinburgh, 5, 111
Reid, M. J., & Menten, K. M. 1990, ApJ, 360, L51
Reid, M. J., & Menten, K. M. 1997, ApJ, 476, 327
Reid, M. J., & Menten, K. M. 2007, ApJ, 671, 2068
Reid, M. J., Menten, K. M., Brunthaler, A., et al. 2009a, ApJ, 693, 397
Reid, M. J., Menten, K. M., Zheng, X. W., et al. 2009b, ApJ, 700, 137
Richards, A. M. S., Yates, J. A., & Cohen, R. J. 1996, MNRAS, 282, 665
Ridgway, S. T., Joyce, R. R., Connors, D., Pipher, J. L., & Dainty, C. 1986, ApJ, 302, 662
Rowan-Robinson, M., & Harris, S. 1983, MNRAS, 202, 767
Rygl, K. L. J., Brunthaler, A., Sanna, A., et al. 2012, A&A, 539, A79
Schönrich, R., Binney, J., & Dehnen, W. 2010, MNRAS, 403, 1829
Schuster, M. T., Humphreys, R. M., & Marengo, M. 2006, AJ, 131, 603
Schuster, M. T., Marengo, M., Hora, J. L., et al. 2009, ApJ, 699, 1423
Shintani, M., Imai, H., Ando, K., et al. 2008, PASJ, 60, 1077
Skrutskie, M. F., Cutri, R. M., Stiening, R., et al. 2006, AJ, 131, 1163
Torres-Dodgen, A. V., Carroll, M., & Tapia, M. 1991, MNRAS, 249, 1
Walborn, N. R. 1973, ApJ, 180, L35
Yates, J. A., & Cohen, R. J. 1994, MNRAS, 270, 958
Zhang, B., Reid, M. J., Menten, K. M., & Zheng, X. W. 2012, ApJ, 744, 23
Zubko, V., Li, D., Lim, T., Feuchtgruber, H., & Harwit, M. 2004, ApJ, 610, 427